

Crystal plasticity finite element simulations of pure bending of aluminium alloy AA7108

A. Saai^{a,b,*}, I. Westermann^{a,b}, S. Dumoulin^{a,b}, O.S. Hopperstad^a

^a SINTEF Materials & Chemistry, NO-7465 Trondheim, Norway

^b Structural Impact Laboratory (SIMLab), Centre for Research-based Innovation (CRI) and Department of Structural Engineering, Norwegian University of Science and Technology, NO-7491 Trondheim, Norway

Abstract

The crystal plasticity finite element method (CP-FEM) is used to investigate the influence of microstructure on the bending behaviour of the heat treatable aluminium alloy AA7108. The study comprises two materials obtained from the AA7108 aluminium alloy by different thermo-mechanical treatments. The first one is an as-cast and homogenized material consisting of large grains with random texture, while the second one is a rolled and recrystallized material having refined grains with weak deformation texture. The behaviour of the two materials in plane-strain bending is investigated numerically and compared qualitatively to existing experimental data. The crystallographic texture and grain morphology of the materials are explicitly represented in the finite element models. The numerical results display a strong effect of the grain morphology on the bending behaviour, the surface waviness and the development of shear bands. These results are consistent with the experimental observations. The simulations further indicate that crystallographic texture affects the bending behaviour of the rolled and recrystallized material.

Keywords: Bending; Aluminium alloy; Microstructure; Crystal plasticity; Finite element models; Shear bands

* Corresponding author Tel.: + 47-73-59- 46-72; fax: + 47-73-59-47-01.

E-mail address: afaf.saai@sintef.no (A. Saai).

1. Introduction

Aluminium is used in the automotive industry instead of steel for an increasing range of components in order to reduce the vehicle weight and thereby to reduce fuel consumption and CO₂ emissions. Aluminium can be formed into complex shapes more easily than steel (e.g. by extrusion). However, substituting aluminium for steel in a car body requires an appropriate combination of strength and ductility with respect to safety. To satisfy these needs, the aluminium alloys are subjected to thermo-mechanical treatments during manufacturing of components and structures. The thermo-mechanical processes modify the microstructure of the alloys, such as crystallographic orientations (texture), grain structure, precipitates, primary particles, and dislocation densities. These changes in the microstructure strongly influence the mechanical properties of the aluminium alloys, including strength, work-hardening, plastic anisotropy and formability. To obtain the desired properties, it is therefore crucial to understand the effects of the thermo-mechanical treatments.

Several systematic experimental studies have been conducted to investigate the influence of the microstructure on the bending formability of aluminium. Snilsberg et al (2010) investigated the bending properties for different orientations of the specimen from the rolling direction for four commercially extruded aluminium alloys with respect to texture and grain structure. Ikawa et al (2010) studied the influence of crystallographic orientation by using experiments with single crystal specimens. Dao and Li (2001) and Westermann et al (2011) revealed the effects of texture, grain morphology and primary-phase particles on bendability and crack propagation.

Modelling of microstructural effects on formability and localization phenomena has been enabled thanks to the application of the crystal plasticity theory to describe the large-strain deformation behaviour of metals and alloys. The microstructural properties have been considered using two approaches. The first one utilizes Taylor-based models (Inal et al, 2002; Kuroda and Tvergaard, 2007; Neale et al, 2003), while the second one uses crystal plasticity theory with explicit representation of the microstructure by use of the finite element method (CP-FEM) (Saai et al, 2010; Rossiter et al, 2010; Hu et al, 2011). Inal et al (2002) and Kuroda and Tvergaard (2007) used a Taylor-based model of crystal plasticity to predict the effect of texture on the formation of shear bands. Neale et al (2003) investigated the effect of through-thickness texture gradients. Hu et al (2008, 2011) emphasized the dominant role of the particles in controlling post-necking deformation using CP-FEM. It should be mentioned here that the grain structure cannot be considered in Taylor-based models. The explicit

representation of the microstructure in CP-FEM promotes the use of this approach to predict localization phenomena from the microstructural inhomogeneities. However, there are limitations on the computing time necessary to handle such simulations. The implied restrictions on the size of the modelled sample prevent the application of this approach in modelling of materials with refined grains or particles.

In the present work, CP-FEM is used to investigate the effect of microstructure on bending behaviour, surface waviness, and initiation and development of shear bands for two materials obtained from an AA7108 aluminium alloy by different thermo-mechanical treatments. While the as-cast and homogenized material has large grains and random texture, the rolled and recrystallized material has finer grains and weak deformation texture. In the finite element model, the grains are explicitly resolved with a refined mesh in order to account for stress and strain gradients with good accuracy.

2. Experiments

The effects of the microstructure on the bendability and the crack propagation in AA7108 materials have been investigated by Westermann et al (2011) using three-point bending tests. The microstructure characteristics obtained in that study were used here as an input for the CP-FEM simulations and are summarized in the following. In the present work, additional experimental characterizations were performed to investigate the effect of the microstructure on the surface waviness of the bending specimens after deformation. These measurements were used for assessment of the FE model.

2.1 Microstructure characteristics

We consider here two of the AA7108 materials studied by Westermann et al (2011). The two materials were obtained from a homogenized AA7108 extrusion ingot subjected to different thermo-mechanical treatments to obtain different microstructures. The microstructure of the two materials, denoted "as-cast and homogenized" and "rolled and recrystallized", was observed by anodizing the samples in a 5% HBF_4 aqueous solution to reveal the grain structure under polarized light (see Figure 1). After solution heat treatment and water quenching, both materials were artificially aged to an underaged condition in a two-step artificial heat treatment: 100° C for 5 hours followed by 150° C for 5 hours. Large equi-axed grains were found in the as-cast and homogenized material. Approximately 36 grains were observed in an area of 1 mm² (Figure 1a). The rolled and recrystallized material exhibits a

refined microstructure, where approximately 1000 grains were observed in an area of 1 mm² (Figure 1b).

The macro-texture of the rolled and recrystallized material was obtained using the electron back scattered diffraction (EBSD) technique and is presented in Figure 2 in the form of {111} and {001} recalculated pole figures and the orientation distribution function (ODF). The ODF was calculated by the EDAX TSL OIM software using a 23 rank harmonic series expansion and average grain orientation weighted by the grain size. Figure 2 shows a very weak texture close to random, with a maximum intensity of 4.4 in the retained deformation texture. The volume fraction of typical deformation and recrystallization texture components have been calculated using the same software (EDAX TSL OIM) and the results are listed in Table 1. Due to the large grain size in the as-cast and homogenized material, the number of grains in the specimen is insufficient for a statistically reliable texture analysis. However, the texture in this material is assumed to be random in accordance with the work of Engler and Hirsch (2009), Hirsch (2012) and Pedersen et al (2015).

2.2 Mechanical Testing

Two types of mechanical tests are important in this work: tensile tests for calibration of the input parameters used in the CP-FEM and three-point, plane-strain bending tests used for qualitative comparisons with the simulated results.

The behaviour of the as-cast and homogenized material is assumed to be independent of direction, and tensile tests were carried out in the longitudinal direction of the ingot. The rolled and recrystallized material was assumed to be anisotropic, and tensile tests were performed in three directions (0°, 45° and 90°) with respect to the rolling direction. The procedure for identifying the parameters of the crystal plasticity model based on the tensile test data is outlined in Section 3. Plane-strain three-point bending tests were performed on specimens with dimensions 50 mm × 50 mm × 2.96 ± 0.09 mm (Westermann et al, 2011). The bending axis was along either the rolling direction (RD) or the transverse direction (TD) for the rolled and recrystallized material. For the as-cast and homogenized material, the bending axis was chosen independently of direction. A brief summary of the most important observations regarding the bendability of the AA7108 alloy is given in the following.

- The force-displacement curves from the three-point bending tests (Figure 3) show that the force level is rather independent of the testing direction for the rolled and recrystallized

material, while a markedly larger displacement to failure is achieved when the bending axis is along TD (an average displacement of 7.9 mm in TD vs. 6.9 mm in RD). Both the force level and the displacement to failure are lower for the as-cast and homogenized material.

- The bending angles at fracture are listed in Table 2 along with the ratio t/R , where t is the thickness and R is the inner bending radius after unloading. Low values of this ratio reflect poor bendability. The as-cast and homogenized material has the poorest bendability, while the bendability of the rolled and recrystallized material depends on the orientation of the bending axis: higher bendability is observed when the bending axis is aligned with TD.
- Figure 4 gives an overview of the crack propagation through the thickness of the specimen. In the case of the as-cast and homogenized material (Figure 4a), the crack path is partly intercrystalline and partly transcrystalline. When the bending axis is parallel to RD for the rolled and recrystallized material (Figure 4b), slant fracture initiates on the tension side of the sample, and as the crack propagates, the mode turns into a mixture of intercrystalline and transcrystalline crack growth, leaving a characteristic zigzag pattern. However, with the bending axis parallel to TD (Figure 4c), the crack propagates from the tension side of the sample as transcrystalline, slant fracture.

2.3 Surface waviness

An optical imaging technique using confocal white light microscopy was used to measure the bending profile on the tensile side of the bending specimens. The specimen surface is illuminated by a white light source and reflects the light which is projected to the microscope's photo-detector. The bending profile of the specimen is then obtained from the height of the scanned surface points compared to a reference surface. In Figure 5, the surface profile is determined for the two materials in two cross-sections centred on the bending axis. The reference length of the surface profile is 4 mm where the bending axis is in the middle of the reference length. The rolled and recrystallized specimen with the bending axis along TD has the largest curvature of the bending profile since this combination of material and orientation gives the best bendability (Table 2). The as-cast and homogenized specimen has poor bendability and exhibits a bending profile with small curvature. Based on the bending profiles, it is found that the surface waviness increases with the grain size of the material. This is consistent with the experimental observations of Dao and Li (2001).

3. Material model

The microstructure of the AA7108 aluminium alloy is explicitly represented in the numerical model using the FE method. The specimen is discretized into a set of grains and each grain is again discretized into a set of elements to obtain a good approximation of the stresses and strains within the grains. The response of each grain is obtained by a rate-dependent single crystal plasticity model (Saai et al, 2013). The work-hardening is modelled by the extended Voce rule which is supposed to capture the yield limit and the shape of the work-hardening curve of aluminium alloys with good accuracy (Guan et al, 2006; Grytten et al, 2008; Prakash et al, 2009). Only the main parts of the constitutive model are presented here; for more details the reader is referred to Saai et al (2013).

For each slip system the relation between the resolved shear stress τ^α and the shear strain rate $\dot{\gamma}^\alpha$ is defined by

$$\dot{\gamma}^\alpha = \dot{\gamma}_0 \left| \frac{\tau^\alpha}{\tau_c^\alpha} \right|^{\frac{1}{m}} \text{sgn}(\tau^\alpha) \quad (1)$$

where τ_c^α is the critical resolved shear stress on system α , and m and $\dot{\gamma}_0$ are material constants representing the microscopic strain-rate sensitivity and the reference shearing rate, respectively. Work-hardening is introduced by making the critical resolved shear stress a function of the plastic straining

$$\dot{\tau}_c^\alpha = \theta(\Gamma) \sum_{\beta=1}^{12} q_{\alpha\beta} |\dot{\gamma}^\beta| \quad (2)$$

where θ defines the hardening rate for a given accumulated plastic strain, $q_{\alpha\beta}$ is the latent hardening matrix and the accumulated plastic shear strain Γ is defined by

$$\dot{\Gamma} = \sum_{\alpha=1}^{12} |\dot{\gamma}^\alpha| \quad (3)$$

The work-hardening rate θ is taken as the derivative with respect to Γ of a master hardening curve in the form

$$\tau_c(\Gamma) = \tau_0 + \sum_{k=1}^N \tau_k \left(1 - \exp\left(-\frac{\theta_k}{\tau_k} \Gamma\right) \right) \quad (4)$$

This is inspired by Tomé et al (1984) who used a similar approach. The work-hardening rate θ is then calculated as

$$\theta(\Gamma) = \frac{d\tau_c(\Gamma)}{d\Gamma} = \sum_{k=1}^N \theta_k \exp\left(-\frac{\theta_k}{\tau_k} \Gamma\right) \quad (5)$$

Here τ_0 is the initial critical resolved shear stress, assumed to be the same for all slip systems, while θ_k and τ_k are the initial hardening rate and saturated value of hardening term k . Two hardening terms are used in this work, i.e. $N = 2$.

The identification of the model parameters for each material is done in the optimization tool LS-OPT (2012) using a finite element model of a representative volume element (RVE) of the material. A periodic RVE composed of 1000 grains is generated and associated to the crystallographic orientations representing the macro-texture. Each grain in the RVE is modelled by one element to reduce the computation time. True stress-strain curves obtained from the tensile tests in the three directions with respect to the rolling direction (cf. Section 2.2) are considered in the calibration process for the rolled and recrystallized material. As mentioned previously, the behaviour of the as-cast and homogenized material is assumed to be independent of direction, and the true stress-strain in the longitudinal direction of the ingot is used. The parameter values obtained for the two materials are given in Table 3. Figure 6 compares the experimental and numerical true stress-strain curves for the two materials. It is seen that the anisotropy of the rolled and recrystallized material is not entirely captured in the simulations. The reason for this is that only crystallographic texture contributes to the anisotropy in the simulations, while in the real material other microstructural features will play a role as well. In particular, the constituent particles are aligned in the rolling direction and may contribute to the mechanical anisotropy.

4. Finite element modelling of bending

Plane-strain elements were used in the finite element model. Each grain was represented by a set of elements associated to a unique initial crystallographic orientation. Four-node square elements were used and the finite element model of each microstructure was generated using Voronoi tessellation. The total number of elements used in each specimen was 54000. These elements were divided into 162 sets of elements (grains) to represent the large grains in the as-cast and homogenized material (Figure 7a). Random orientations were associated to these

grains. For the rolled and recrystallized material the mesh was divided into 4500 sets of elements (Figure 7b), where each set was associated to one initial crystallographic orientation from the measured texture for this material.

A plate with unit width, thickness $H = 3$ mm and length $L = H/2$ was modelled by CP-FEM, see Figure 8. To obtain a pure bending state in the plate, the vertical edges $X = 0$ and $X = L$ were given a rotation around the midpoints of each edge with constant angular speed $\dot{\Phi} = 0.23^\circ/\text{sec}$ (Kuroda and Tvergaard, 2004; Triantafyllidis et al, 1982). The boundary conditions applied to the nodes along these edges are expressed by:

$$\begin{aligned} u_x \cos\left(\pm \frac{\Phi}{2}\right) - \left(u_y + y - \frac{H}{2}\right) \sin\left(\pm \frac{\Phi}{2}\right) &= 0, \\ q_x \sin\left(\pm \frac{\Phi}{2}\right) + q_y \cos\left(\pm \frac{\Phi}{2}\right) &= 0 \end{aligned} \quad (6)$$

where u_x and u_y are, respectively, the displacement along the X and Y axes, y is the Y coordinate of the node, Φ is the bending angle, q_x and q_y are in turn the X and Y components of the traction force normal to the edge (given per current area). The plus sign in front of Φ holds for $X = L$ and the minus sign holds for $X = 0$. The thickness direction of the plate is always along the Y axis, whereas the Z axis represents the bending axis. These boundary conditions thus represent pure bending.

The FE simulations were performed with the explicit solver of LS-DYNA, using mass scaling to reduce the computation time. It was carefully checked that the dynamic effects were at all times negligible, so that the simulations could be considered to be quasi-static.

5. Results and discussion

The predicted bending moment versus bending angle curves for the two materials are plotted in Figure 9. A slight difference in the bending moment is observed for the two different directions of the rolled and recrystallized material, while the as-cast and homogenized material exhibits the lowest bending moment. The bending moment could not be calculated from measurements made in the three-point bending tests performed by Westermann et al (2011) and we can only make qualitative comparisons with these experiments. However, the force-displacement curves from the bending tests show the same trend with respect to the different materials (see Figure 3). Similar force level is observed for the two different

directions of the rolled and recrystallized material, while the as-cast and homogenized material exhibits significantly lower force.

Deformed grains with contours of accumulated plastic strain are represented in Figure 10 for both materials. In Figure 11, the plastic strains at three different bending angles are extracted for the elements in two sections: the first one is close to the free surface and the second one is at 0.73 mm from the free surface of the bending specimen. The deformed sections are presented on the specimen in Figure 10 as black lines. Shear bands, here defined as narrow zones of intense plastic straining, are initiated on both the tension and compression sides of the sample and propagate inside the grains and along the grains boundaries. As can be observed, the large grain size of the as-cast and homogenized material leads to the formation of wide shear bands. Non-uniform deformation within the shear bands is induced by the different orientations between neighbouring grains (see Figure 11). The plastic deformation is self-organized into crossed shear bands inclined at around 45° to the free surface of the specimen for the rolled and recrystallized material. These crossed bands are found on both the tension and compression sides (see Figure 10). It is also found that the spacing between the shear bands is smaller than for the as cast and homogenised material due to the refined size of the grains.

The largest accumulated plastic strains are organized in shear bands at an earlier stage of deformation, i.e., at a low value of the bending angle, for the as-cast and homogenized material (see Figure 10). This could explain the low bendability compared to the rolled and recrystallized material, cf. Table 2. The largest accumulated plastic strains are observed when the bending axis is along the rolling direction for the rolled and recrystallized material (see Figure 10). This anisotropy ensues in the CP-FEM simulations from the influence of the weak deformation texture observed in this material (Table 1). This is consistent with numerical simulations of strain localization in textured aluminium materials by Tvergaard and Needleman (1993), Dao and Li (2001) and Kuroda and Tvergaard (2006).

Figure 12 shows a close-up of the tensile side of the rolled and recrystallized specimens for the two orientations of the bending axis. Discontinued shear bands are obtained in the FE simulations due to the different orientations of neighbouring grains. Dao and Li (2001) showed that a shear band in an aluminium sheet material could jump over a grain before continuing further if this grain has non-favourable crystallographic orientation for deformation. This crystallographic orientation-dependent deformation is one of the mechanisms inducing the zigzag shape of the fracture observed in Figure 4. The fracture

could initiate and develop in a shear band and then it could change path to follow a crossing shear band where the grains have favourable orientations for deformation (Figure 12). In the simulations, this mechanism is observed for the rolled and recrystallized material for both bending directions, i.e. the shear bands develop in the same way. However, the experimental observations show that the cracks propagate differently in this material with respect to the orientation of the bending axis (Figure 4). This is linked to the non-homogenous distribution of the primary particles, which are broken up and aligned with the rolling direction (Westermann et al, 2011). The position and distribution of primary particles are known to affect the initiation and development of shear bands in aluminium alloys (Dao and Li, 2001; Hu et al, 2008; 2011). The influence of the primary particles was not considered in the present study because this would require a characteristic element size less than the average size of the primary particles and thus lead to excessive computation times. A macro-micro-multi-level modelling scheme was proposed by Hu et al (2010) to investigate numerically the effect of particle distribution on wrap-bendability of AA5754 alloys and could be a solution to overcome this limitation.

In Figure 13, the predicted maximum value of the accumulated plastic strain in the bending sample is plotted against the t/R ratio for the two materials, where t is the plate or sheet thickness and R is the inner bending radius. The marker \times indicates the maximum plastic strain corresponding to the t/R value measured at the end of the experimental bending test. At the same t/R ratio, the highest value of the accumulated plastic strain is predicted for the as-cast and homogenized material that exhibits the lowest bendability (see Table 2). High values of plastic strain are related to the large grain size in this material. In the case of the rolled and recrystallized material, the simulations show that the maximum accumulated plastic strain at the same t/R ratio is consistently larger when the bending axis is parallel to RD which corresponds to the direction with the lowest bendability for this material (see Table 2). It should be noted here that the simulation with the bending axis parallel to TD could not be run to the value of t/R giving failure in the experiments due to numerical instability (at high bending angle, high pressure is obtained in the elements on the compression side of the specimen due to the refined mesh).

Figure 14 shows the free surfaces of the bending specimens obtained by CP-FEM at the same bending angle (17°). The two materials exhibit strong surface waviness on the tensile and compression sides of the specimen. The numerical model predicts an increase of the waviness of the profile surface with an increase in grain size in agreement with the experiments (see

Figure 5). The shear bands are initiated in the two materials from some of the local troughs on the free surfaces resulting from the surface waviness. As mentioned previously, the development of shear bands depends on the crystallographic orientation of the grains and shear bands could be initiated from grains on the surfaces having favourable crystallographic orientations for deformation.

6. Concluding remarks

The crystal plasticity finite element method was used to predict the effects of the microstructure of an AA7108 aluminium alloy on the bending moment, the surface waviness and the initiation and development of shear bands during plane-strain bending. The study comprised two materials obtained from the AA7108 aluminium alloy by different thermo-mechanical treatments. The as-cast and homogenized material has large grains and random texture, whereas the rolled and recrystallized material has finer grains and weak deformation texture.

It was found that early organization of the deformation into shear bands took place during bending of the as-cast and homogenized material, leading to higher level of the maximum plastic strain at given bending radius than for rolled and recrystallized material. For the rolled and recrystallized material the highest level of maximum plastic strain at a given bending radius was found when the bending axis was along the rolling direction, as a result of the crystallographic texture of this material. A high value of the predicted maximum plastic strain in the numerical simulations was found to correlate with low bendability in the experiments. The surface waviness predicted by the finite element model increased with the grain size in good agreement with the experimental observations.

Large shear bands were observed for the as-cast and homogenized material, which propagated through the grains and along the grain boundaries. The shear bands were denser in the rolled and recrystallized material due to the refined grains. Non-uniform deformations were observed in the shear bands in both materials and linked to the misorientation between neighbouring grains. This non-uniform deformation in the shear bands is one of the mechanisms explaining the zigzag shape of the crack path observed experimentally. The fracture could initiate and develop in a shear band and then change path to follow a crossing shear band where the grains had more favourable orientations for deformation. In the simulations with CP-FEM, the propagation of shear bands in the rolled and recrystallized material was not affected by the crystallographic texture. However, experimental observations

showed that cracks propagate differently in this material with respect to the orientation of the bending axis. This is attributed to the non-homogenous distribution of the primary particles. To account for this behaviour in the simulations, the FE model would have to account for the size and distribution of the primary particles, which play an important role in the crack propagation.

Acknowledgement

The authors gratefully acknowledge the financial support of this work from the Structural Impact Laboratory (SIMLab), Centre for Research-based Innovation (CRI) at the Norwegian University of Science and Technology (NTNU) and the generous technical assistance of Dr. Torodd Berstad, Dr. Nuria Espallargas and Shawn Wilson.

References

- Bold, H., Plättchen-Biegeversuch, PAPP PWT 4108, Daimler Chrysler, Sindelfingen, Germany, Feb. 2004.
- Dao, M., Li, M., A micromechanics study on strain-localization-induced fracture initiation in bending using crystal plasticity models. *Philosophical Magazine A* 81 (2001) NO. 8, 1997-2020
- Engler O., and Hirsch., J., Control of recrystallisation texture and texture-related properties in industrial production of aluminium sheet. *International Journal of Materials Research* 100 (2009) 564-575
- Ikawa, S., Asano, M., Kuroda, M., Yoshida, K., Effects of crystal orientation on bendability of aluminum alloy sheet. *Materials Science and Engineering A* 528 (2011) 4050-4054
- Inal, K., Wu, P.D., Neale, K.W., Finite element analysis of localization in FCC polycrystalline sheets under plane stress tension. *International Journal of Solids and Structures* 39 (2002) 3469-3486
- Hirsch., J., Textures in Industrial Processes and Products. *Materials Science Forum* 702-703 (2012) 18-25

- Hu, X.H., Wilkinson, D.S., Jain M., Wu, P.D., Mishra, R.K., The impact of particle distributions and grain-level inhomogeneities on post-necking deformation and fracture in AA5754 sheet alloys during uniaxial tension. *Materials Science and Engineering A* 528 (2011) 2002-2016
- Hu, X.H., Jain, M., Wilkinson, D.S., Mishra, R.K., Microstructure-based finite element analysis of strain localization behavior in AA5754 aluminum sheet. *Acta Materialia* 56 (2008) 3187-3201
- Hu, X.H., Jain, M., Wilkinson D.S., and Mishra, R.K., A macro-micro-multi-level modeling scheme to study the effect of particle distribution on wrap-bendability of AA 5754 sheet alloys, *J. Mater. Proc. Tech.* 210, 2010, 1232-1242.
- Kalidindi, S.R., Bronkhorst, C.A., Anand, L., 1992. Crystallographic texture evolution in bulk deformation processing of FCC metals. *Journal of the Mechanics and Physics of Solids* 40, 537-569
- Kuroda, M., Tvergaard, V., Effects of texture on shear band formation in plane strain tension/compression and bending. *International Journal of Plasticity* 23 (2007) 244-272
- Kuroda, M., Tvergaard, V., Shear band development in anisotropic bent specimens. *European Journal of Mechanics A/Solids* 23 (2004) 811-821
- LS-DYNA, Version 971, Livermore Software Technology Corporation, Livermore (2012)
- LS-OPT, Version 4.2, Livermore Software Technology Corporation, Livermore (2012)
- Metzger, D.R., Duan, X., Jain, M., Wilkinson, D.S., Mishra, R., Kim, S., Sachdev, A.K., The influence of particle distribution and volume fraction on the post-necking behaviour of aluminium alloys. *Mechanics of Materials* 38 (2006) 1026-1038
- Neale, K.W., Inal, K., Wu, P.D., Effects of texture gradients and strain paths on localization phenomena in polycrystals. *International Journal of Mechanical Sciences* 45 (2003) 1671-1686
- Pedersen, K.O., Westermann, I., Furuc, T., Børvika, T., Hopperstad, O.S., Influence of microstructure on work-hardening and ductile fracture of aluminium alloys. *Materials & Design* 70 (2015) 31–44

- Rossiter, J., Brahme, A., Simha, M.H., Inal, K., Mishra, R., A new crystal plasticity scheme for explicit time integration codes to simulate deformation in 3D microstructures: Effects of strain path, strain rate and thermal softening on localized deformation in the aluminum alloy 5754 during simple shear. *International Journal of Plasticity* 26 (2010) 1702-1725
- Saai, A., Dumoulin, S., Hopperstad, O.S., Lademo, O.-G., Simulation of yield surfaces for aluminium sheets with rolling and recrystallization textures. *Computational Materials Science* 67 (2013) 424-433
- Saai, A., Louche, H., Tabourot, L., Chang H.J., Experimental and numerical study of the thermo-mechanical behavior of Al bi-crystal in tension using full field measurements and micromechanical modeling. *Mechanics of Materials* 42 (2010) 275-292
- Tomé, C., Canova, G.R., Kocks, U.F., Christodoulou, N., Jonas, J.J., The relation between macroscopic and microscopic strain hardening in FCC polycrystal. *Acta Metall.* 32 (10) (1984) 1637–1653.
- Triantafyllidis, N., Needleman, A., Tvergaard, V., On the development of shear bands in pure bending. *International Journal of Solids and Structures* 18 No.2 (1982) 121-138
- Tvergaard, V., Needleman, A., Shear band development in polycrystals. *Proceedings of the Royal Society of London A*443 (1993) 547–562
- Westermann, I., Snilsberg, K.E., Sharifi, Z., Hopperstad, O.S., Marthinsen, K., Holmedal, B., Three-point bending of heat-treatable aluminum alloys: influence of microstructure and texture on bendability and fracture behavior. *Metallurgical and Materials Transactions A* 42 (2011) 3386-3398
- Snilsberg, K.E., Westermann, I., Holmedal, B., Hopperstad, O.S., Langsrud, Y., Marthinsen, K., Anisotropy of bending properties in industrial heat-treatable extruded aluminum alloys, *Materials Science Forum* 63-642 (2010), 487-492

Legends

Figure 1 Micrographs illustrating the microstructure of a) the as-cast and homogenized material and b) the rolled and recrystallized material.

Figure 2 Macro-texture of the rolled and recrystallized material represented as a) $\{001\}$ and $\{111\}$ recalculated pole figures and b) orientation distribution function (ODF).

Figure 3 Force-displacement curves from the three-point bending tests.

Figure 4 Crack propagation in a) the as-cast and homogenized material, b) the rolled and recrystallized material with the bending axis \parallel RD and c) the rolled and recrystallized material with the bending axis \parallel TD.

Figure 5 Bending profile for the two investigated materials

Figure 6 True stress-true strain curves from CP-FEM and tensile tests for the as-cast and homogenized material, and the rolled and recrystallized material in three directions with respect to the rolling direction

Figure 7 Finite element model for a) the as-cast and homogenized material and b) the rolled and recrystallized material.

Figure 8 Boundary conditions used in the numerical model to represent plane-strain bending test.

Figure 9 Bending moment per unit width for the as-cast and homogenized material, the rolled and recrystallized material with the bending axis \parallel RD, and the rolled and recrystallized material with bending axis \parallel TD.

Figure 10 Deformed grains with contours of plastic strain for the as-cast and homogenized material, the rolled and recrystallized material with the bending axis \parallel RD, and the rolled and recrystallized material with bending axis \parallel TD

Figure 11 Plastic strains at three different bending angles in two sections: a) close to the free surface on the tensile side of the specimen and b) at 0.73 mm from this surface.

Figure 12 Shear bands development on the tensile side of the rolled and recrystallized material with a) the bending axis \parallel RD and b) the bending axis \parallel TD

Figure 13 Maximum plastic strain in the sample versus thickness to bending radius ratio for the three cases of bending test considered in this study. The marker (\times) indicates the maximum plastic strain corresponding to the value measured at the end of the experimental bending test.

Figure 14 Free surface of the specimen on the tensile and compression sides for the three considered cases of the bending test

Tables:

Table 1 Surface fraction of typical deformation and recrystallization texture components in the rolled and recrystallized material

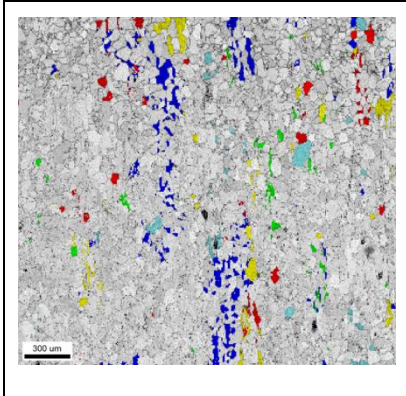
	Texture component	Surface Fraction
	■ Copper: {112}[111]	0.027
	■ Brass: {011}[211]	0.016
	■ S: {123}[634]	0.011
	■ Cube: {100}[001]	0.011
	■ Goss: {110}[001]	0.007

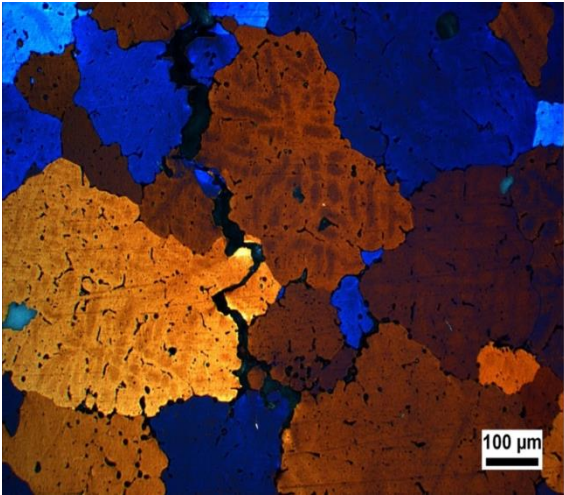
Table 2 Measured bending angles and thickness to bending radius ratios at fracture from three-point plane-strain bending tests

Material	Bending Axis	Average Bending Angle [°]	Standard Deviation [°]	t/R [-]
As-cast and homogenized	—	22	2.5	0.33
Rolled and recrystallized	// RD	49	2.1	0.97
	// TD	61	1.0	1.61

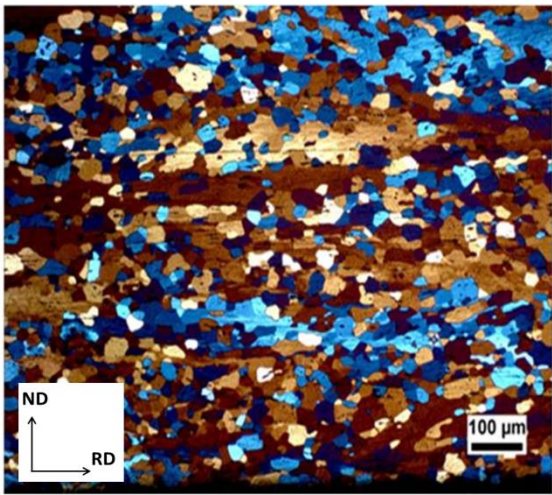
Table 3 Model parameters for the two materials

Parameter	As-cast and homogenized	Rolled and recrystallized
$\dot{\gamma}_0$ (s ⁻¹)	0.001	0.001
m	5×10^{-3}	5×10^{-3}
$q_{\alpha\beta}$	1.0 if $\alpha = \beta$ 1.4 if $\alpha \neq \beta$	1.0 if $\alpha = \beta$ 1.4 if $\alpha \neq \beta$
τ_0 (MPa)	136.0	142.9
θ_1 (MPa)	4.5×10^6	6.5×10^5
τ_1 (MPa)	1.0	1.0
θ_2 (MPa)	42.5	53.1
τ_2 (MPa)	2.0×10^5	8.6×10^3

Figures:



a)



b)

Figure 1. Micrographs illustrating the microstructure of a) the as-cast and homogenized material and b) the rolled and recrystallized material.

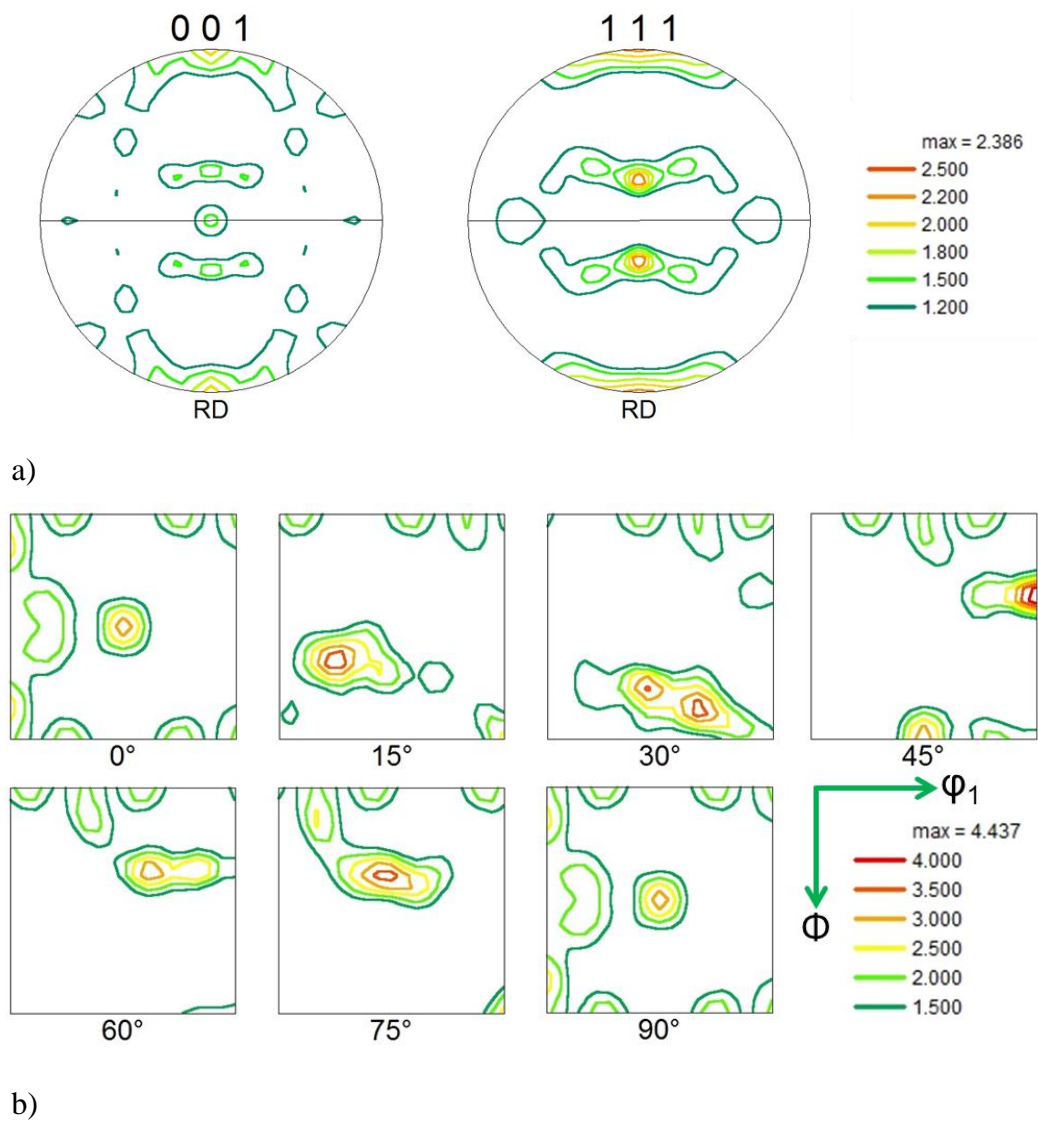


Figure 2. Macro-texture of the rolled and recrystallized material represented as a) $\{001\}$ and $\{111\}$ recalculated pole figures and b) orientation distribution function (ODF).

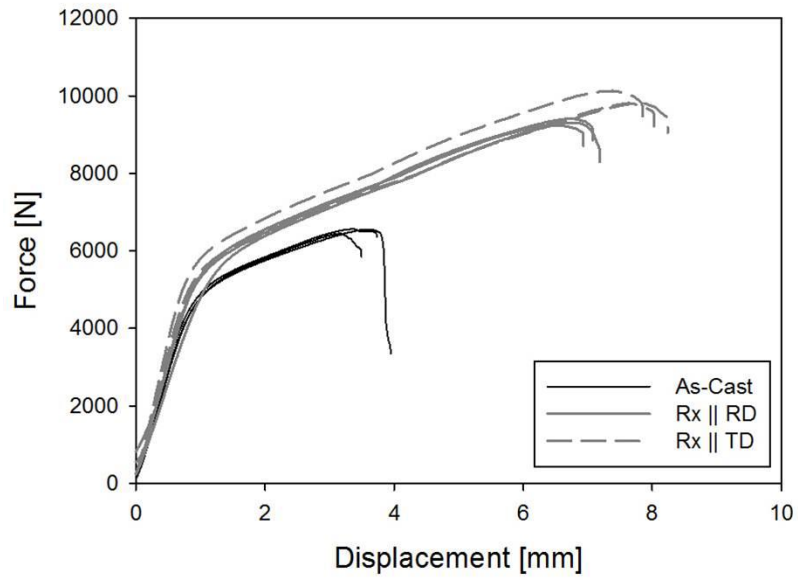
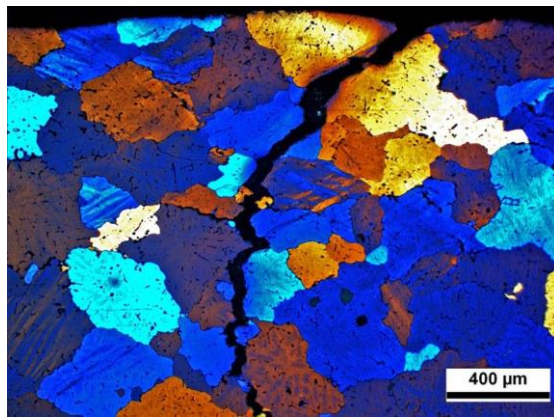
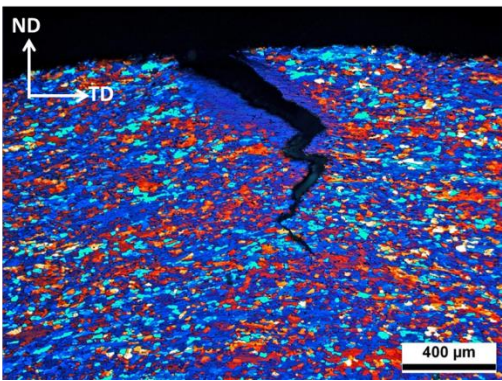


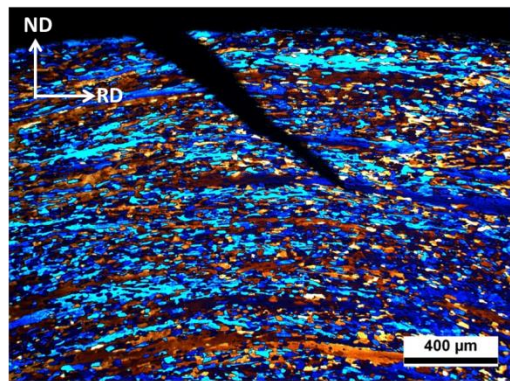
Figure 3. Force-displacement curves from the three-point bending tests.



a)



b)



c)

Figure 4. Crack propagation in a) the as-cast and homogenized material, b) the rolled and recrystallized material with the bending axis \parallel RD and c) the rolled and recrystallized material with the bending axis \parallel TD.

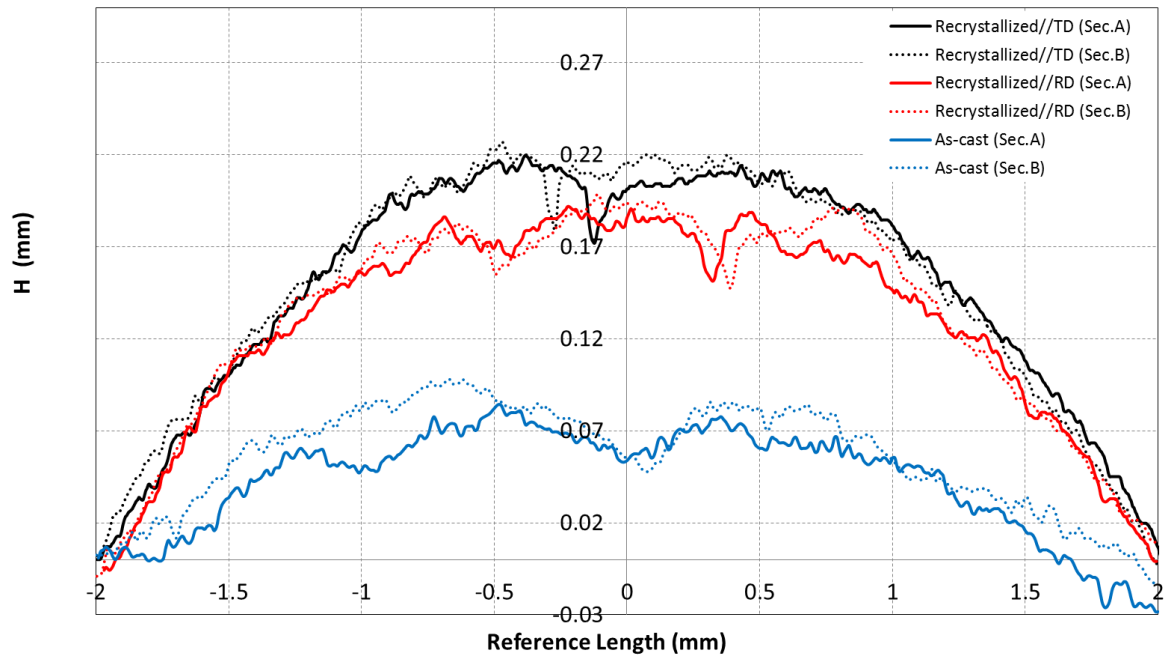


Figure 5. Bending profile for the two investigated materials

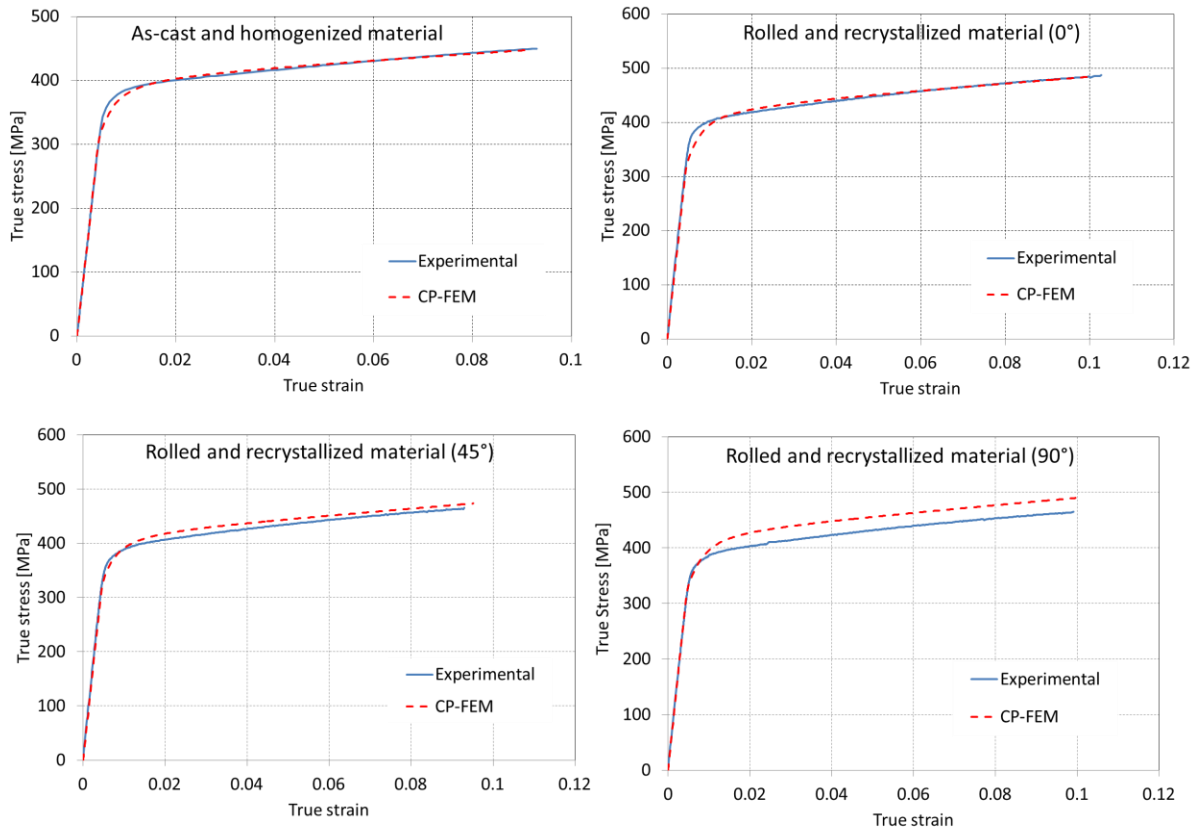


Figure 6. True stress-true strain curves from CP-FEM and tensile tests for the as-cast and homogenized material, and the rolled and recrystallized material in three directions with respect to the rolling direction

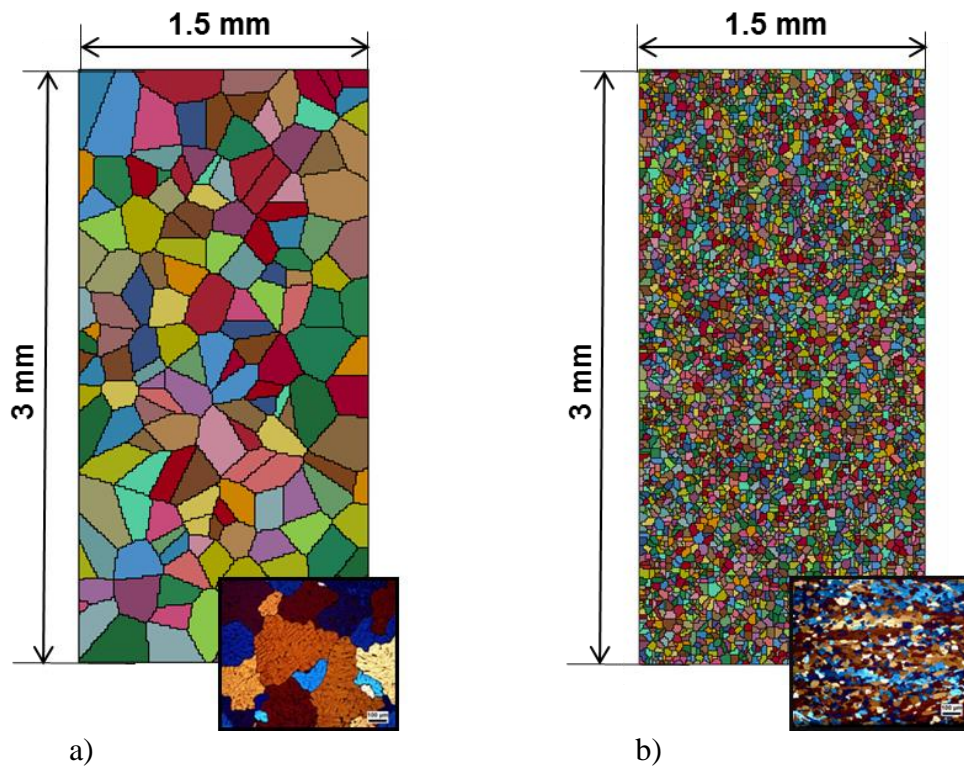


Figure 7. Finite element model for a) the as-cast and homogenized material and b) the rolled and recrystallized material.

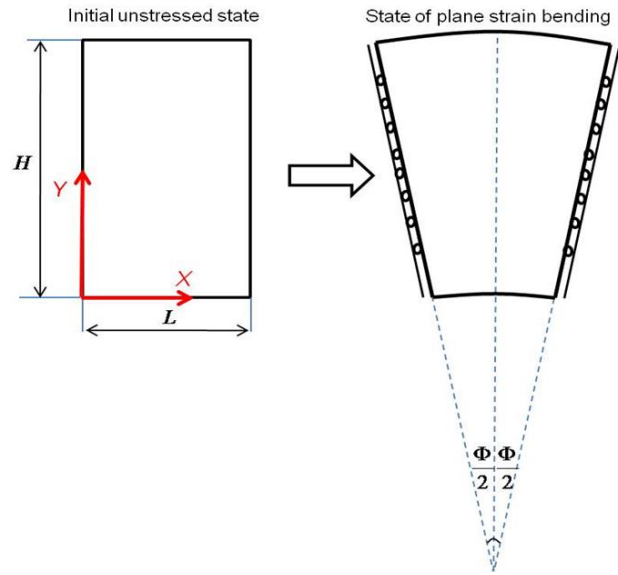


Figure 8. Boundary conditions used in the numerical model to represent plane-strain bending test.

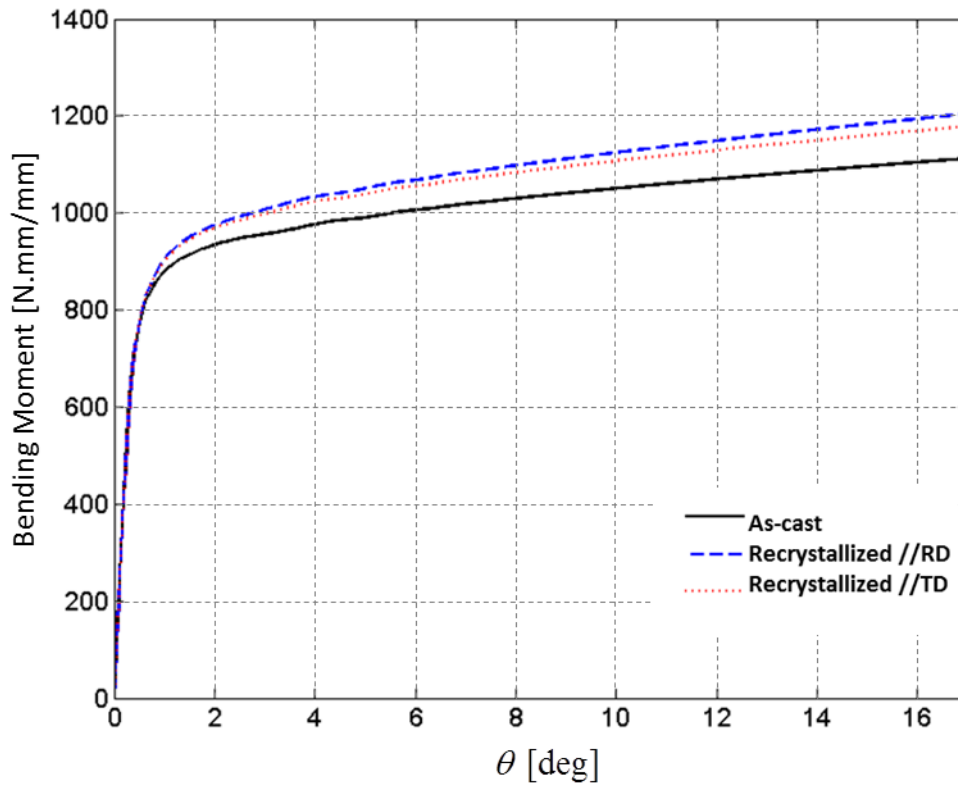


Figure 9. Bending moment per unit width for the as-cast and homogenized material, the rolled and recrystallized material with the bending axis \parallel RD, and the rolled and recrystallized material with bending axis \parallel TD.

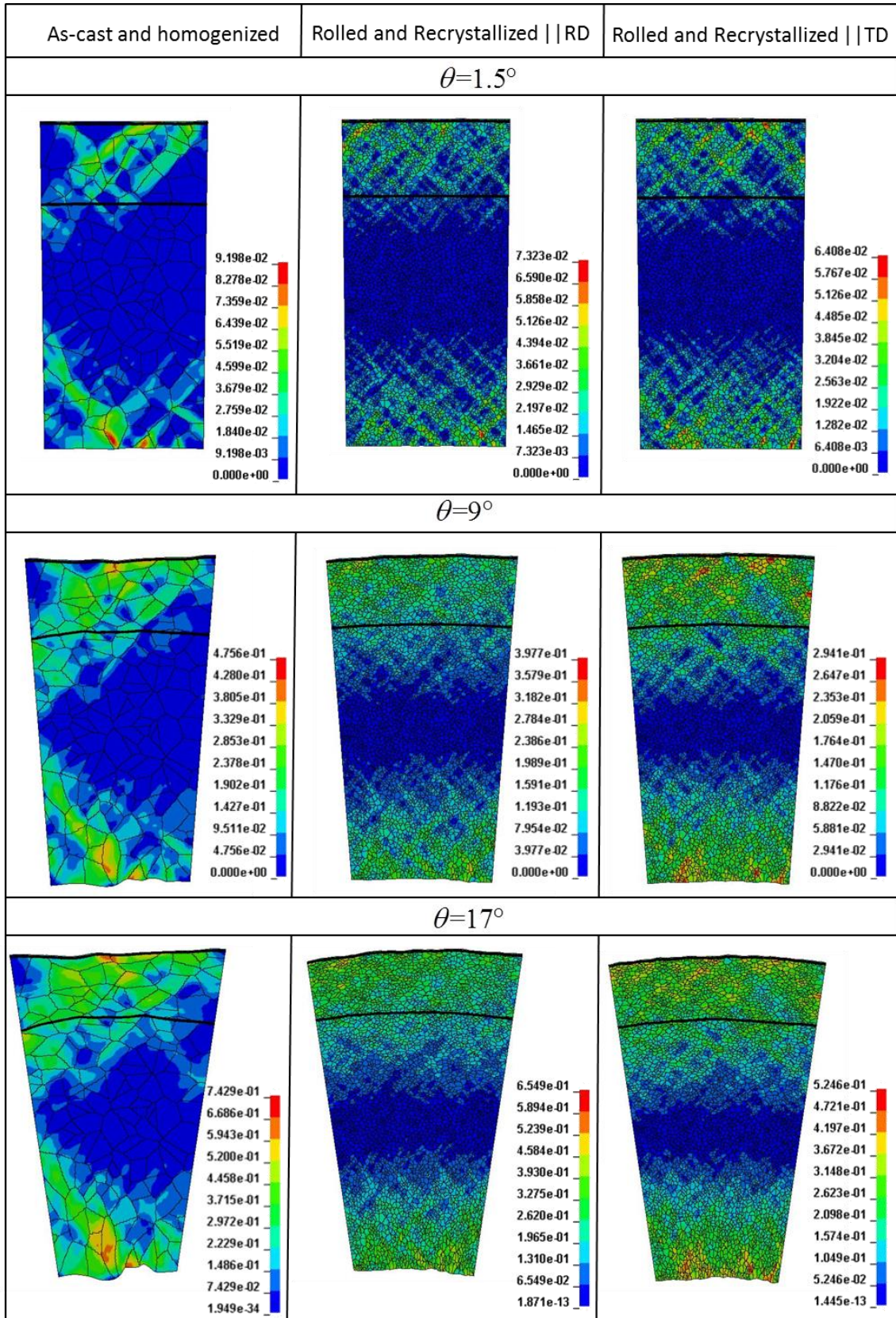


Figure 10. Deformed grains with contours of plastic strain for the as-cast and homogenized material, the rolled and recrystallized material with the bending axis || RD, and the rolled and recrystallized material with bending axis || TD. Note that different ranges have been used for the contours of the plastic strain.

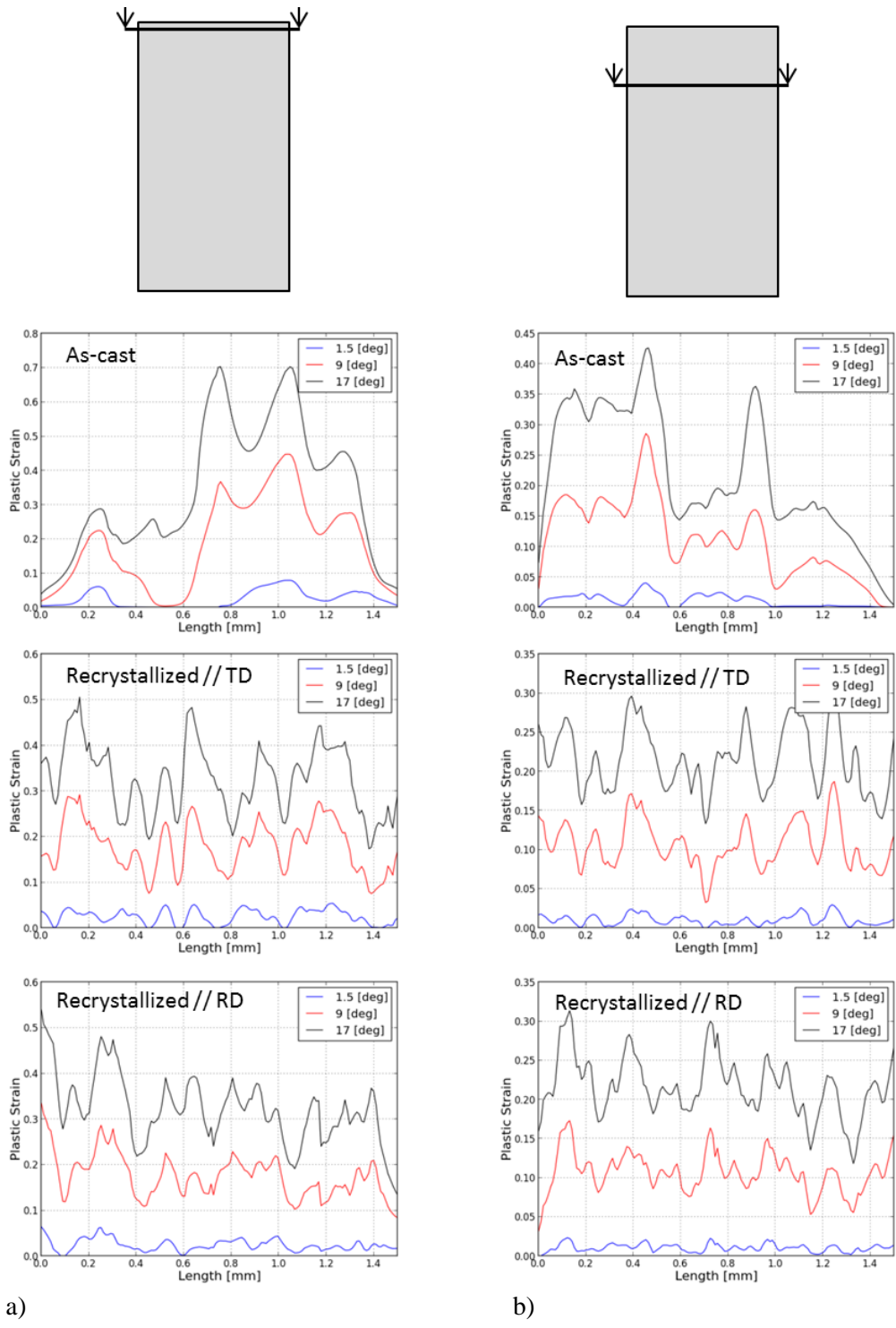
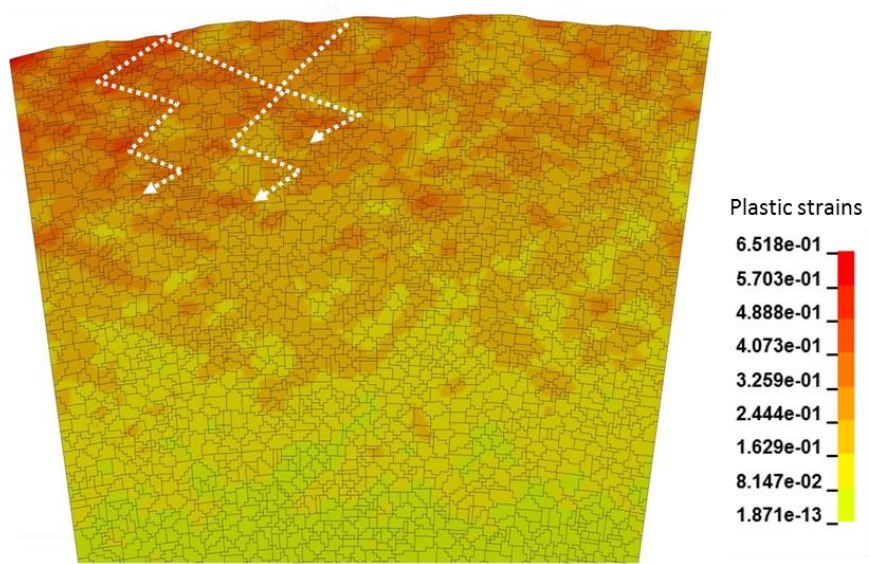
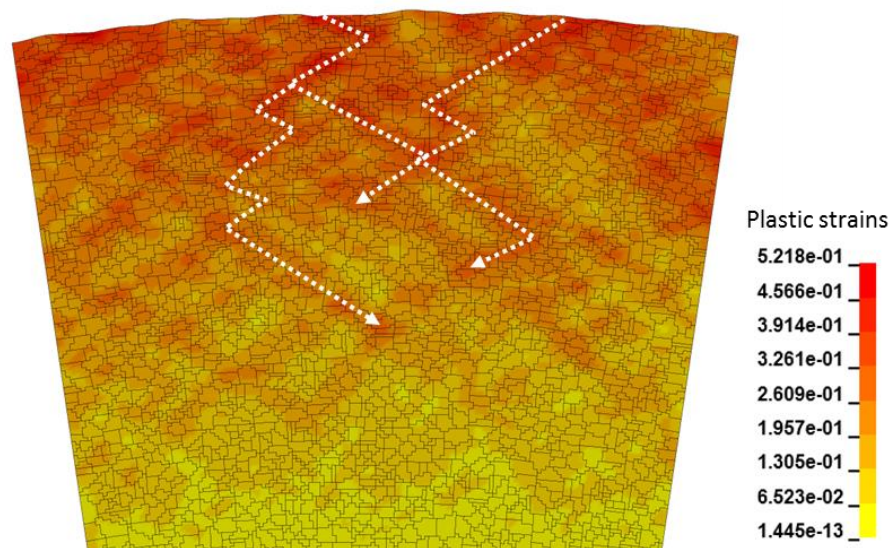


Figure 11. Plastic strains at three different bending angles in two sections: a) close to the free surface on the tensile side of the specimen and b) at 0.73 mm from this surface.



a)



b)

Figure 12. Shear bands development on the tensile side of the rolled and recrystallized material with a) the bending axis \parallel RD and b) the bending axis \parallel TD

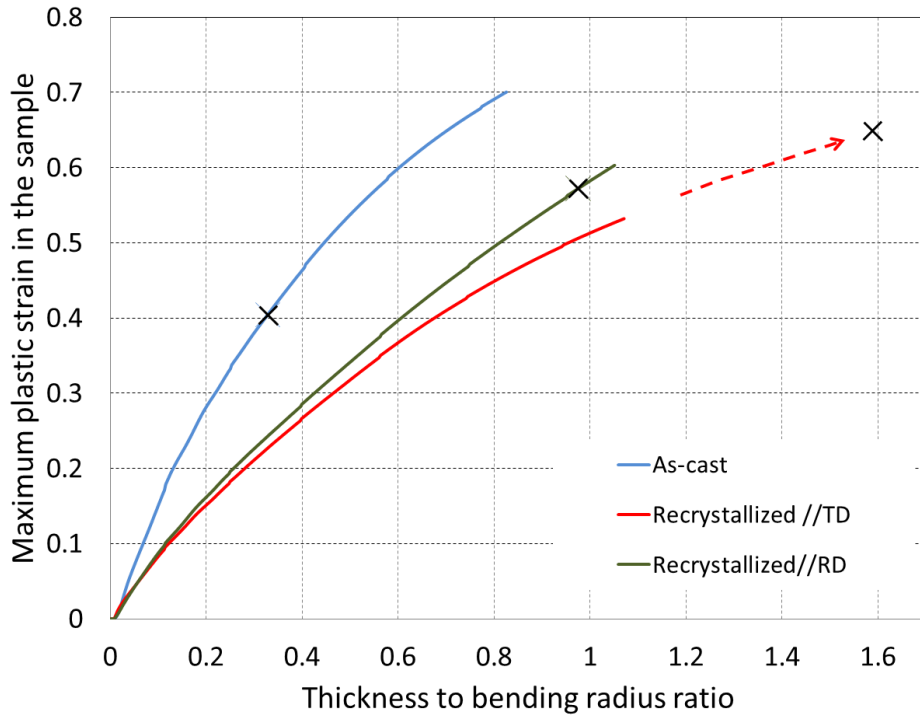


Figure 13. Maximum plastic strain in the sample versus thickness to bending radius ratio for the three cases of bending test considered in this study. The marker (x) indicates the maximum plastic strain corresponding to the value measured at the end of the experimental bending test.

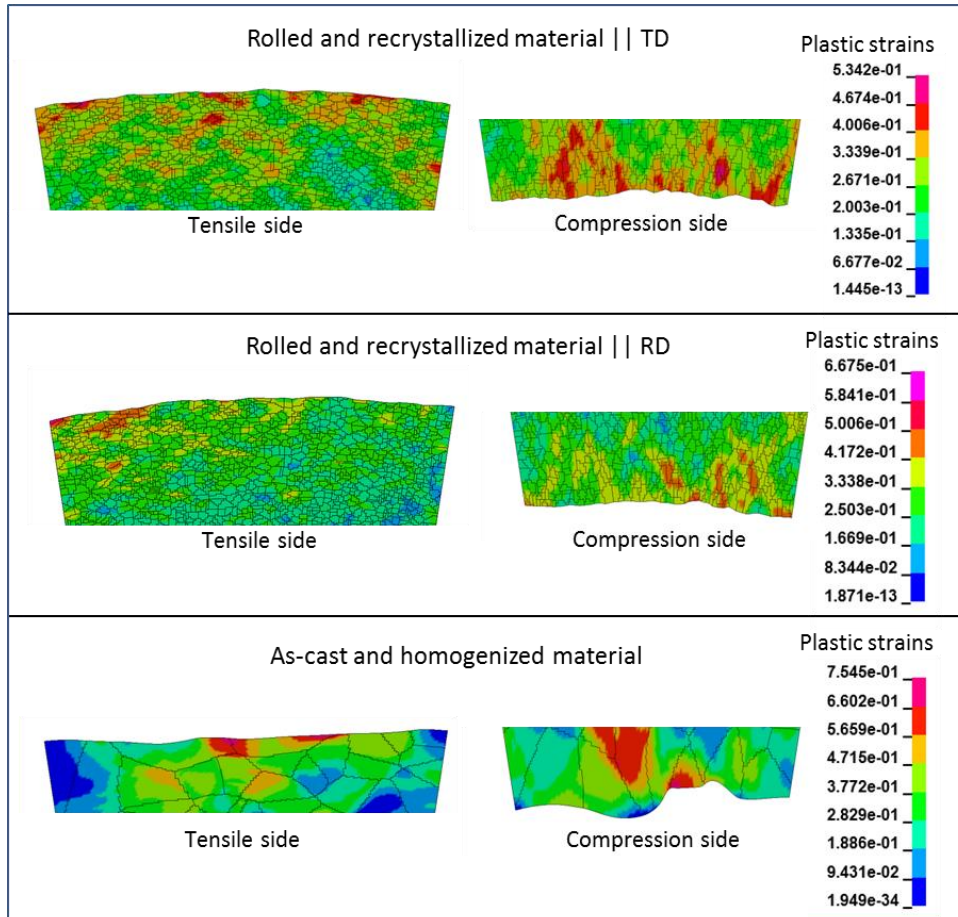


Figure 14. Free surface of the specimen on the tensile and compression sides for the three considered cases of the bending test